

4. Structural response of $\text{La}_2\text{Zr}_2\text{O}_7$ pyrochlore upon irradiation with 1.0 MeV Xe^{4+} ions

4.1 Introduction

The material characteristics and their response to the adverse environment are of utmost interest in several fields for diverse applications such as high-temperature SOFCs, immobilization of nuclear wastes, buffer layer coating on superconductors, *etc.* [1–3]. As per the earlier studies, material characteristics can be driven by engineering the composition, annealing time duration and temperature, pressure, and so on [4,5].

Pyrochlore compounds, $\text{A}_2\text{B}_2\text{O}_7$, feature an extensive diversity of compositions because of their feasible and flexible structure. The capability of structural feasibility and flexibility of $\text{A}_2\text{B}_2\text{O}_7$ compounds has been established it, a promising candidate for astonishing applications in diverse technological fields such as immobilization of radioactive nuclides, electrocatalysis, magnetic, optical, solid oxide fuel cell, thermal barrier coatings, *etc.* [3,6–8]. Here, it is imperative to mention that the engineering of the B-site rare earth element altered the ferroelectricity, ionic conductivity, luminescence, and radiation tolerance of pyrochlore compounds [9]. The alteration of these properties in pyrochlore compounds is associated with the emergence of disordering due to engineering the A- and B-sites cations [9].

Moreover, the order-disorder transformation and crystalline to amorphous phase can achieve easily through pressure and energetic ion beam irradiation [1,9]. In pyrochlore compounds, the $\text{La}_2\text{Zr}_2\text{O}_7$ (LZO) is a standout material because of its stability and suitability in diverse kinds of technologically important fields [8,10]. The structural defects in the LZO system can be induced by composition, pressure, and ion beam irradiation [11]. The induced structural disordering of LZO pyrochlore is beneficial for several emerging applications in different areas such as scintillator, photocatalysis, buffer coating on superconductors, high-temperature SOFCs, ferroelectricity, and so on [2,3,7,8,12]. Previous studies have evaluated the solubility and stability of the actinides in the LZO system and reported that the embodiment of Pu enhanced the radiation stability of LZO [13]. Mustafa et al. reported that the LZO is a crucial material for capacitive applications due to its structure scalability and feasibility [10]. Recently, Ou et al. observed the two-order higher conductivity for mixed-phase LZO system [8].

Therefore, form inspiring the properties of LZO and feasible use for societal development and advancement; here, we have investigated the response of structural behaviour

of LZO at two different temperatures, i.e. 300 K and ~ 88 K upon irradiation of 1.00 MeV Xe^{4+} ions. Accordingly, the present chapter deals with the structural assessment of LZO samples upon irradiation 1.0 MeV Xe^{4+} at room temp. (300 K) and low temp. (~ 88 K) as a function of ion fluence ($1.0\text{E}13$, $5.0\text{E}13$, and $1.0\text{E}14$ ion.cm^{-2}). The synthesis method, ion irradiation process and characterizations techniques employed here have been explained in detail in chapter 2.

4.2 Results and Discussion

4.2.1 FE-SEM study

FE-SEM has been employed to examine the microstructure of the virgin $\text{La}_2\text{Zr}_2\text{O}_7$ (LZO) sample. Fig. 4.1 (a) shows the FE-SEM micrograph of the virgin LZO sample. A broad range (80-250) of grain sizes is observed employing the rectangular intercept technique and Image J software [14]. The rectangular intercept technique has been explained in chapter 3 in the section of FE-SEM analysis.

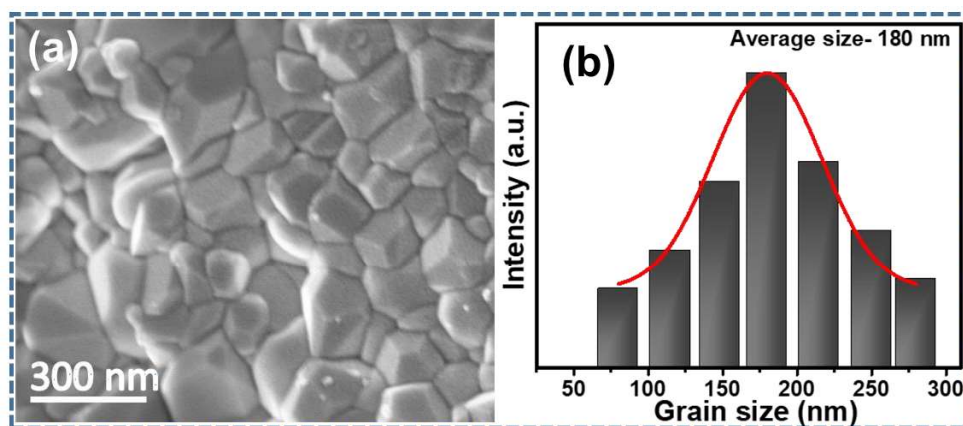


Figure 4.1 FE-SEM micrograph of virgin LZO sample (a) and (b) size histogram.

The grains and grain boundaries are clearly visible which seem associated with the higher grain size and disappearance of porosity in the LZO sample. Employing the Gaussian fitting, the size distribution of the virgin LZO sample was quantified which is presented in Fig. 4.1 (b). The average grain size of the virgin LZO sample is found to be 180 nm.

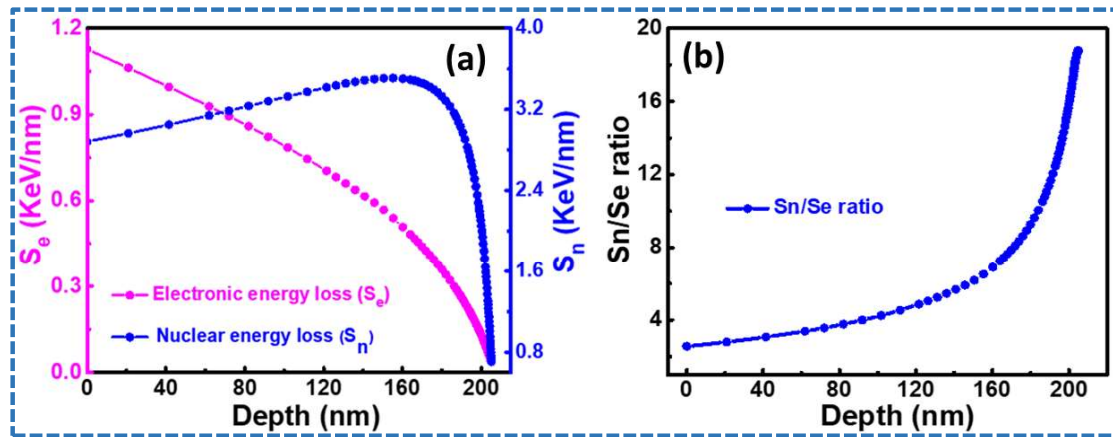


Figure 4.2 Illustration of S_e and S_n plot (a) and S_n/S_e ratio plot in respect of depth of ion irradiated LZO.

4.2.2 SRIM simulation

The nuclear energy loss (S_n) and electronic energy loss (S_e) of LZO samples upon irradiation of 1.0 MeV Xe^{4+} ions at different fluences have been quantified employing the SRIM 2003 [15]. Fig. 4.2 (a) exhibits that the S_n and S_e are 2.9 keV/nm and 1.12 keV/nm for the LZO sample. The S_n/S_e ratio plot specifies that the S_n is ~ 2.5 times greater as compared to the S_e [Fig. 4.2 (b)]. The ion fluence, dose, and irradiation parameters have been portrayed in the section of irradiation experiments of chapter 2.

4.2.3 GIXRD analysis

To investigate the impact of 1.0 MeV Xe^{4+} ions irradiation at room temperature, RT (300 K), and low temperature (~ 88 K) as a function of ion fluences, i.e., $1.0\text{E}13$, $5.0\text{E}13$, and $1.0\text{E}14$ ion/cm², the GIXRD technique has been performed. Fig. 4.3 (a, d) exhibits the GI-XRD patterns of before and after ion irradiated LZO samples in respect of three different fluences. The response of GIXRD reflections of LZO samples is found to be corroborated with the earlier studies [16,17]. The reduction in the intensity of reflections is observed at both temperatures as a function of ion fluence. The diminution of reflections intensity specifies the degradation of the crystallinity of LZO samples [16]. The broadening and weakening of the GIXRD reflections of LZO samples are found to be relatively higher for ~ 88 K [Fig. 4.3 (b, e)]. The relatively widened and weakened reflections of LZO samples at ~ 88 K indicate that the degradation of crystallinity is quite higher at ~ 88 K than 300K. Here, it should be addressed that the defects are mobile at RT while defects are immobile at low temperature [18]. Therefore, the relatively lower damage/degradation in the crystallinity of LZO samples with the augmentation of ion fluence upon irradiation at 300 K may be associated with the mobility of

defects, i.e., recovery of defects at 300 K. Fig. 4.3 (c, f) exhibits the enlarged view of superstructure reflections, i.e., (331) and (511) of pyrochlore phase. The presence of superstructure reflections in LZO samples suggests that upon irradiation of 1.0 MeV Xe⁴⁺ ions all samples possess the pyrochlore phase structure at both the temperature.

Previous studies stated that LZO favored the cation disorder and it should be radiation resist upon ion irradiation with the formation of order-disorder (pyrochlore to defect fluorite transition) phenomenon [4,19]. The critical dose of amorphization enhances with the enhancement of the irradiation temperature, and above the critical temperature, the absolute amorphization cannot be obtained in the materials [20]. In situ TEM measurements of LZO samples, upon ion irradiation of 1.5 MeV Xe⁺ ion suggests that the LZO become amorphized at the dose of 5.5 dpa at RT instead of formation of defect fluorite structure [20]. Here, we wish to stress that the irradiation dose of LZO samples is two order lesser than the critical amorphization dose (5.5 dpa). Therefore, the GIXRD reflections specify the pyrochlore phase upon irradiation of 1.0 MeV Xe⁴⁺ ions.

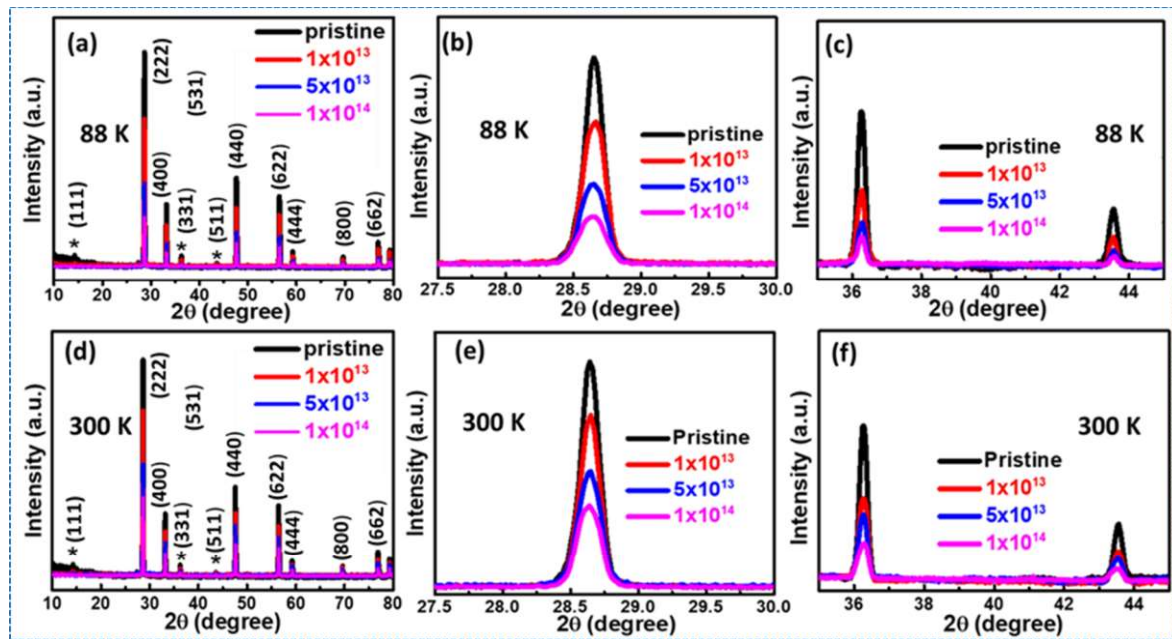


Figure 4.3 GI-XRD patterns of before and after irradiated LZO samples (a, d); enlarged view of (222) reflection (b, e) and (c, f) superstructure reflections, i.e., (331) and (511).

Further, employing the expression, $\beta^2 = \beta_{exp}^2 - \beta_{inst}^2$, we evaluate the intensities and widths (FWHM) of the LZO samples at both temperatures. Both, the intensity and width of (222) reflections appear irradiation temperature and ion fluence dependent as shown in Fig. 4.4 (a-b). It is found that the intensity of (222) reflection decreases at both the temperatures with the enhancement of the fluence [Fig. 4.4 (a)] and diminution in the intensity of (222) reflection

is found to be less at 300 K than ~88 K. In addition, the peak broadening of the (222) reflection increases in respect of ion fluence at 300 K and ~88 K. Moreover, augmentation in peak broadening of the (222) reflection is relatively lower at 300 K which suggest that the degradation of the crystallinity is relatively lower at 300 K in comparison of ~88 K, i.e., LZO samples irradiated at 300 K possess low damage than the LZO samples irradiated at ~88 K [Fig. 4.4 (a-b)]. The lesser damage in the LZO samples upon irradiation at 300 K appears may be associated with recombination, migration, and diffusion of defects [18].

Previous studies reported that the degradation of crystallinity, emergence of defects, and dislocations are major factors in the materials for the broadening of reflections [15,21]. Debelle et al. found that the lattice stain emanates from the deterioration of crystallinity and emergence of defects in the compounds due to pressure, temperature, and irradiation [15]. Therefore, we would like to emphasize that the ion irradiation-induced defects and lattice strain essentially originate the peak broadening in the LZO samples. Employing the Stokes and Wilson expression, $\varepsilon = \beta / 4 \tan \theta$, the ion irradiation-induced lattice strain in the samples was determined [21]. Fig. 4.4 (c) exhibits the lattice strain of pre and post irradiated LZO samples. It is found that the lattice strain of the samples enhances monotonically with the enhancement of ion fluence at both the temperatures. The quantified lattice strain is found to be relatively higher at ~88 K as compared to 300 K. These results suggest that the peak broadening in the LZO samples is associated with the emergence of lattice strain due to the ion irradiation phenomenon. It is generally accepted that the widening of the XRD peaks is the measure of deterioration of the crystallinity. The irradiation-induced damage/amorphization in the compounds can be determined by the relative variation in the full-width half maxima (FWHM) [22]. The ion irradiation-induced damage/ amorphization was quantified employing the following equation.

$$Damage = \frac{FWHM_{(222) \text{ irradiated}} - FWHM_{(222) \text{ pristine}}}{FWHM_{(222) \text{ pristine}}} \quad (4.1)$$

Where, $FWHM_{(222) \text{ irradiated}}$ is the FWHM of (222) reflection post-irradiation and $FWHM_{(222) \text{ pristine}}$ is the FWHM of (222) reflection before irradiation.

The damage quantified employing the equation 4.1, is found to be more pronounced at ~88 K than 300 K, i.e., the impact of ion irradiation is more prominent at low temperature. Table 4.1 summarized the ion irradiation-induced damage of LZO samples at both the temperatures. Qing et al. obtained the monotonically decrement in the intensity and progressive increment in FWHM of the XRD peaks of $\text{Nd}_2\text{Zr}_2\text{O}_7$ samples with the enhancement of ion fluence (4.08×10^{13} to 5.28×10^{16} ions/cm²) upon irradiation of Xe^{20+} ions (2.0 MeV) [16].

The ion irradiation-induced damage/amorphization of Nd₂Zr₂O₇ samples enhanced with the augmentation of ion fluence. Li et al. irradiated the polycrystalline Er₂Ti₂O₇ samples with 400 keV Ne²⁺ ions.

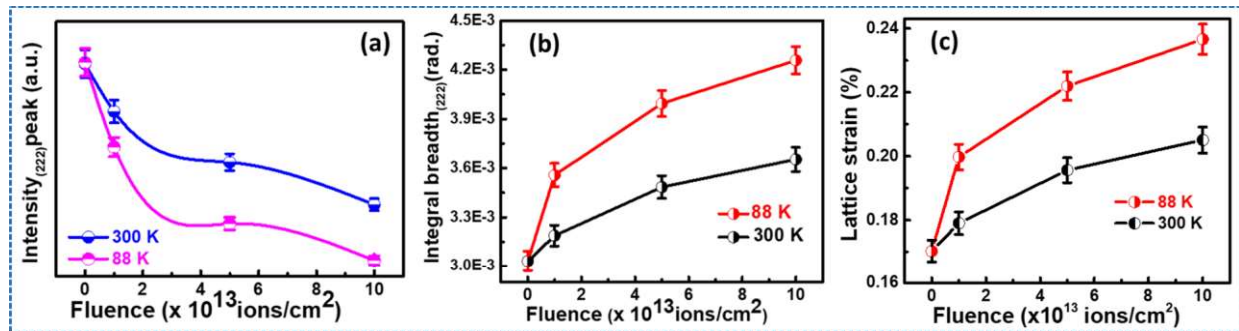


Figure 4.4 Illustration of intensity (a), FWHM (b), and (c) strain with the enhancement of ion fluence.

It has been reported that the deterioration of crystallinity or/and amorphization phenomenon is enhanced with the augmentation of the ion fluence (1.0E18 to 2.0E19 ions/cm²) [23]. The polycrystalline Ti₂AlC and Te₃SiC₂ samples has been irradiated at three different temperatures (300 K, 630 K, and 973 K) and found that the damage/amorphization monotonically decreases with the increase of irradiation temperature [24]. Moreover, the SrTiO₃ single crystals over the temperatures range from 150 K to 400 K were irradiated with 1.0 MeV Au ions by Zhang et al. [25]. As expected, the ion irradiation disorder/amorphization decreased with the enhancement of the irradiation temperature from 140 K to 400 K. Zhang et al. stated that with the enhancement of irradiation temperature, the recombination, migration, and diffusion of defects are movable. Therefore, the occurrence of disordering/amorphization is significantly higher at lower temperature [25].

Table 4.1 Summarized the damage quantified from the GIXRD and Raman spectroscopy of LZO samples.

Sample code	Damage (GIXRD)		Damage (Raman)	
	300 K	~88 K	300 K	~88 K
Pristine	-	-	-	-
1.0×10 ¹³ ions/cm ²	11%	16%	14%	20%
5.0×10 ¹³ ions/cm ²	17%	27%	23%	32%
1.0×10 ¹⁴ ions/cm ²	28%	39%	34%	43%

Schrempel et al. stated that the critical damage/amorphization dose for irradiated LiNbO₃ single crystals is much lower upon irradiation at 15 K due to the immobility of induced

defects [26]. In contrast, the critical damage/amorphization dose is found to be higher at RT as compared to lower temperature (15 K) due to mobilization of defects, i.e., damage/amorphization depends on the irradiation temperature [26].

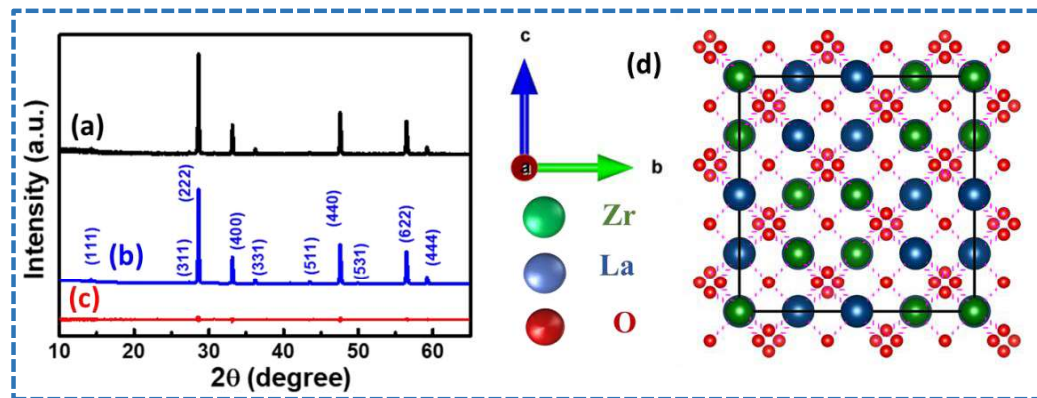


Figure 4.5 Represents the GIXRD pattern of virgin LZO (a), (b) calculated pattern, and (c) disparity of observed and calculated pattern; (d) crystal structure of LZO.

The disordering/amorphization altered with the function of irradiation temperature and ion fluence. The irradiation temperature plays a crucial role in the recovery of defects. It is well accepted that with the enhancement of the irradiation temperature the defects become immensely movable, i.e., the defects mobility rates enhanced with the augmentation of irradiation temperature and results in, materials exhibiting relatively less damage/amorphization at higher temperature compared to lower temperature [22,24,25].

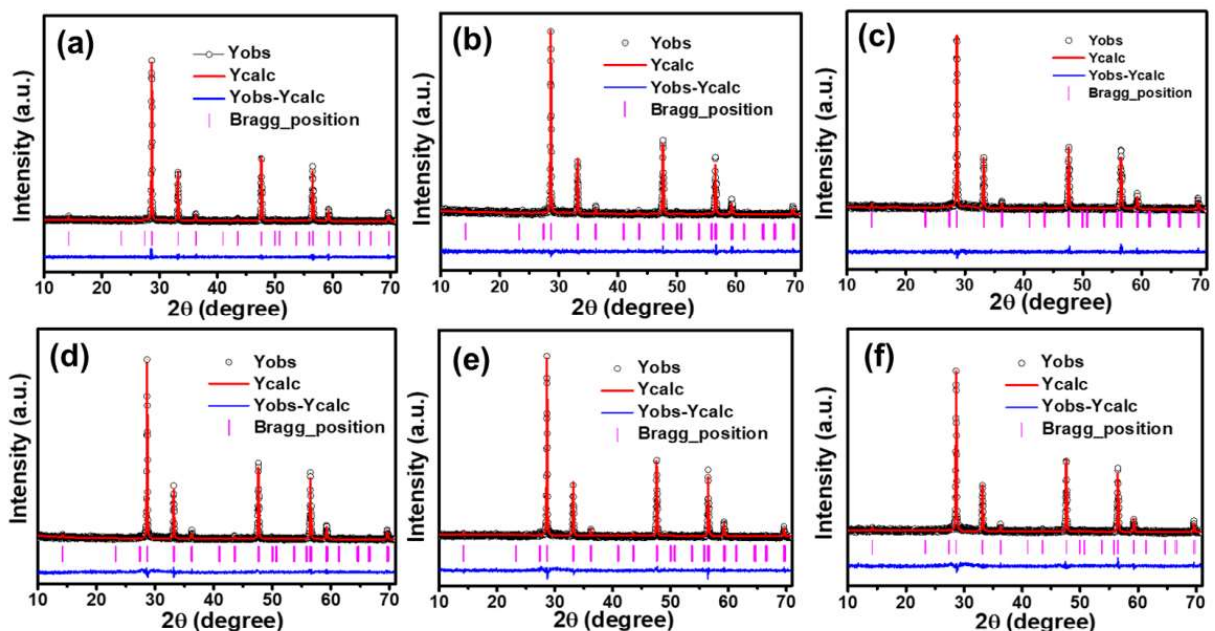


Figure 4.6 Rietveld refinement of the post irradiated LZO samples at ~88 K (a-c) and (d-f) 300 K with the fluence of 1.0×10^{13} , 5.0×10^{13} , and 1.0×10^{14} ions/cm².

Earlier studies confirmed that the ion irradiation-induced disorder, defects/dislocations, and damage/amorphization (deterioration of crystallinity) is significantly influenced by the ion fluence and irradiation temperature. The concurrently weakening and broadening in the XRD peaks are associated with the irradiation temperature and ion fluence, i.e., both the parameters make a significant contribution in the emergence of degradation of crystallinity or/and amorphization of compounds [18,25,26].

Table 4.2 Structural parameters of the pre and post-irradiated LZO samples.

Sample	300 K				88 K			
	Pristine	1x10 ¹³	5x10 ¹³	1x10 ¹⁴	Pristine	1x10 ¹³	5x10 ¹³	1x10 ¹⁴
Space group	<i>Fd$\bar{3}m$</i>							
Lattice constant	10.789(2)	10.792(1)	10.794(1)	10.796(2)	10.789(2)	10.795(2)	10.799(1)	10.801(1)
R_B	8.77	9.76	9.45	8.96	8.77	9.89	11.29	10.20
R_{wp}	11.9	12.01	13.23	13.49	11.9	12.32	12.78	13.10
R_{exp}	8.98	9.43	9.67	10.21	8.98	8.87	9.87	11.43
χ^2	1.75	1.62	1.87	1.75	1.75	1.92	1.67	1.31

In the present study, we found the concurrently broadening and weakening in the XRD peaks of LZO samples with the augmentation of fluence at both the temperatures, which suggests the emanates of damage/amorphization (degradation of crystallinity). The concurrently broadening and weakening in the XRD peaks may be associated with the increased irradiation dose/fluence. Further, we wish to emphasize that the damage is found to be relatively more pronounced at ~88 K in comparison of 300 K, i.e., deterioration of crystallinity is significantly more pronounced at ~ 88 K. The more prominent deterioration of crystallinity in LZO samples irradiated at ~ 88 K may be related with the immovable nature of defects at low temperature. Therefore, we conclude that the damage is more noticeable at low temperature (~88 K) than RT due to the subjugation of defects recovery phenomenon.

4.2.4 Rietveld analysis

To get more detailed information about the phase and crystal structure, the Rietveld refinement of pre and post irradiated LZO samples was performed employing the Fullprof program [27–29]. Fig. 4.5 (a-c) exhibits the Rietveld refinement of the un-irradiated LZO sample. The presence of superstructure reflections [Fig. 4.5 (a-b)] certainly specifies the formation of the pyrochlore phase of the LZO sample. Figure. 4.5 (d) demonstrates the schematic representation of the crystal structure of the pyrochlore phase LZO sample, which

suggests that the LZO sample has a pyrochlore phase with the space group of $Fd\bar{3}m$. Moreover, we refined the XRD patterns of post irradiated LZO samples to quantified the phase and lattice parameters. Fig. 4.6 illustrates the Rietveld refinement of the post irradiated LZO samples at ~ 88 K and 300 K with the enhancement of ion fluence (e.g., $1.0E13$, $5.0E13$, and $1.0E14$). The Rietveld analysis of all samples suggests that all samples possess the pyrochlore phase with a cubic crystal structure. Table 4.2 presented the Rietveld refined parameters (e.g., R_B , R_{exp} , R_{wp} , and χ^2) and lattice constants for all samples. Table 4.2 shows that the lattice parameters of LZO samples increase monotonically with the enhanced fluence at ~ 88 K and 300 K. Here, we would like to mention that the direct proportional relation in the lattice parameter and strain is reported by the Qin et al. [30]. As we mentioned above, the lattice strain of LZO samples enhanced monotonically with the augmentation of the fluence at both the temperatures. Therefore, we assume that the enhancement in the lattice parameter of all samples upon irradiation may be related to the ion irradiation-induced lattice strain.

4.2.5 Analysis of vibrational mode: Raman spectroscopy

As we have discussed in the section of analytical/experimental techniques of chapter 2, Raman spectroscopy is a non-destructive and prominent tool to examine the vibrations modes of compounds [31]. The Raman spectroscopy measurements have been performed to investigate the impact of ion irradiation on the vibrational modes of LZO samples. Fig. 4.7 (a-b) associates the Raman spectra of pre and post irradiated LZO samples at two different temperatures. It is noteworthy that the pyrochlore, $A_2B_2O_7$, compounds have six Raman active modes. These six Raman active vibrational modes can be depicted as [32].

$$\Gamma = A_{1g} + E_g + 4F_{2g} \quad (4.2)$$

However, the fluorite structure ($Fm\bar{3}m$) has only a single Raman active vibrational mode. The presence of four Raman active modes in the range of 150 to 700 cm^{-1} suggests the constitution of the pyrochlore phase in all LZO samples [Fig. 4.7 (a-b)]. We deconvoluted the Raman spectra of the LZO sample (irradiated with the fluence of $1.0E13$ ions/ cm^2) for both the temperatures [Fig. 4.7 (c-d)]. Deconvolution of Raman spectra suggests that the Raman active vibrational modes, i.e., F_{2g} (1), F_{2g} (2), F_{2g} (3), and A_{1g} mode are positioned at ~ 298 , ~ 396 , ~ 496 , and ~ 518 cm^{-1} , respectively. Further, the deconvolution of Raman spectra indicates that the vibrational mode positioned at ~ 298 cm^{-1} is the combination of two modes, i.e., F_{2g} (1) and E_g modes [Fig. 4.7 (c-d)]. These two modes appeared from the vibration of oxygen in the ZrO_6 octahedron. The Raman modes, F_{2g} (2) and F_{2g} (3) are associated with O-Zr-O bending and Zr-O stretching vibrations. The Raman mode, A_{1g} , arises due to La-O stretching [32,33].

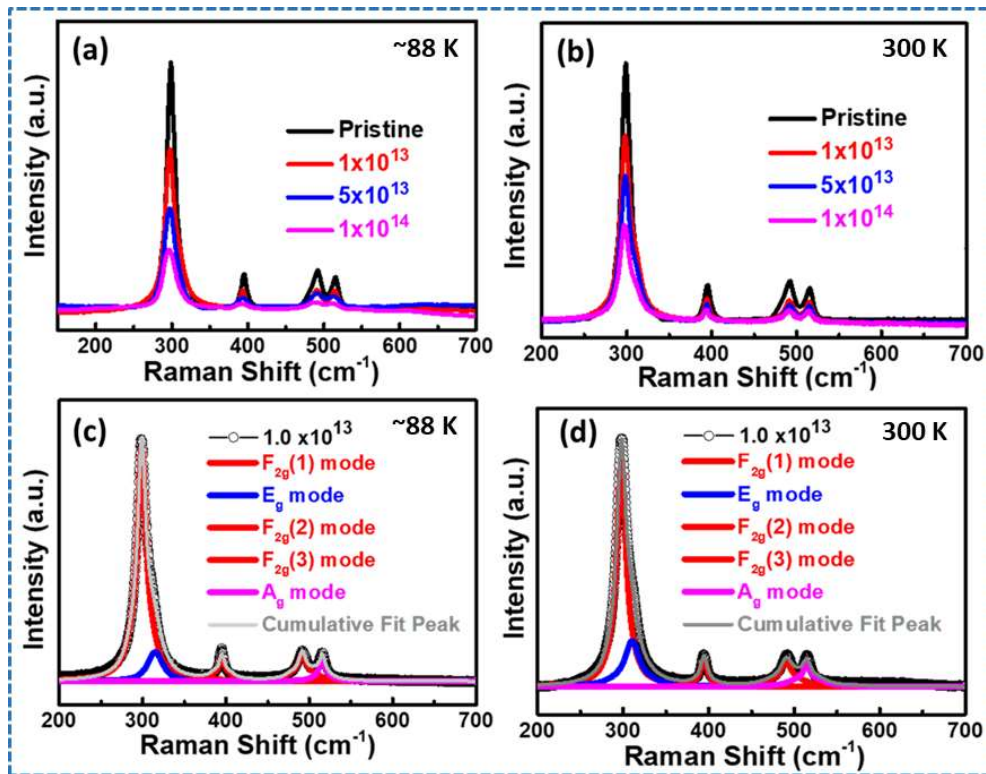


Figure 4.7 Raman spectra of irradiated LZO sample (a) ~ 88 K and (b) 300 K; (c-d) illustrates the deconvoluted Raman spectra of the LZO sample ($1.0E13$ ions/cm²).

Fig. 4.7 (a-b) shows that the vibrational modes of post irradiated LZO samples are weakened and broaden with the increment of fluence at ~ 88 K and 300 K. The weakened and broadened vibrational modes of LZO samples indicates that the vibrational modes deteriorated with the function of ion fluence. Upon irradiation of higher fluence, the vibrational modes situated at higher frequencies side (496 and 518 cm⁻¹) present the broad nature with some extent of discernible.

Therefore, we calculated the intensity and FWHM of the vibrational modes of pre and post irradiated LZO samples as displayed in Fig. 4.8 (a-b). Fig. 4.8 (a) exhibits that the FWHM of the vibrational modes at both the temperatures enhances with the function of ion fluence, whereas the intensity of vibrational modes decreases monotonically. The concurrently broadening and weakening of the vibrational modes evidently indicates the deterioration of vibrational modes, i.e., vibrational modes being distorted upon irradiation. In the pyrochlore compounds, the disorder is an intrinsic phenomenon that is related to the existence of defects and vacancies in the pyrochlore compounds [34].

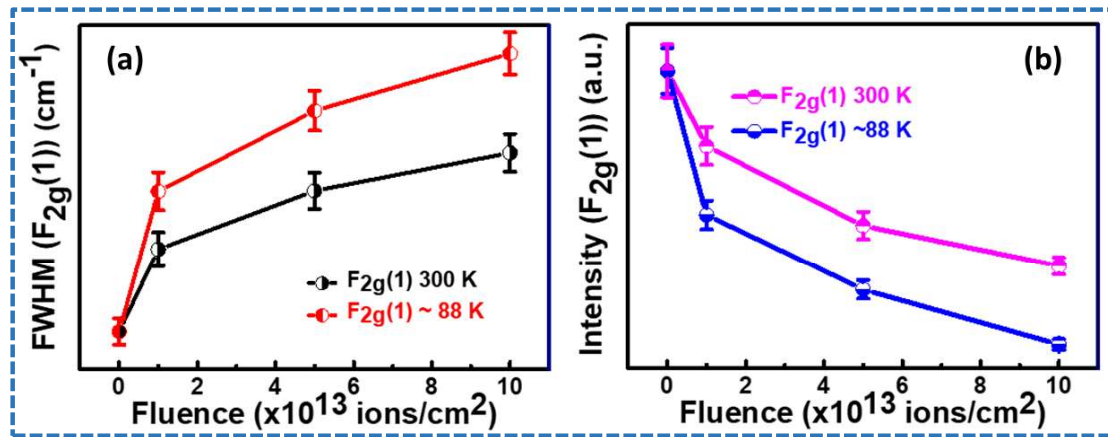


Figure 4.8 Represents the FWHM (a) and (b) intensity of vibrational modes with the function of fluence at two different temperatures.

However, the significantly pronounced broadening and weakening in the vibrational modes in the irradiated LZO samples compared to the un-irradiated LZO sample specifies the ion irradiation-induced deterioration of vibrational modes, which is well corroborated with earlier results [16,33]. Recently, Shu et al. found that the vibrational modes become weakened and broadened upon ion irradiation and stated that the weakened and broadened vibrational modes designate significant distortions and deterioration of associated chemical bonds [35]. Zhang et al. reported the broadening and weakening of the vibrational modes of LZO samples upon irradiation of Kr ions due to the formation of ion irradiation-induced disorders [33]. Therefore, in the present study, we assume that the weakening and broadening of vibrational modes with the function of fluence at ~88 K and RT are associated with ion irradiation-induced deterioration of vibrational modes. The relatively broadened and weakened vibrational modes at ~88 K in comparison of RT suggest the more pronounced deterioration and disordering in the corresponding vibrational modes.

Table 4.3 Depicts the vibrational mode frequencies and assigned vibrational mode of pre and post irradiated LZO samples.

Pristine	300 K			88 K			Assigned mode
	1x10 ¹³	5x10 ¹³	1x10 ¹⁴	1x10 ¹³	5x10 ¹³	1x10 ¹⁴	
298.96	298.49	298.17	296.14	297.57	297.04	296.33	F _{2g} (1)+ E _g
395.62	394.46	394.27	393.95	393.54	392.77	392.66	F _{2g} (2)
491.94	490.98	491.48	491.43	490.69	490.42	488.94	F _{2g} (3)
515.47	514.70	515.21	513.71	513.84	512.39	510.61	A _g

Table 4.3 shows the variation in the vibrational mode frequencies of un-irradiated and irradiated LZO samples. Table 4.3 exhibits the red-shift of vibrational modes for all LZO samples. The shifting of vibrational modes is attributed to the deformation of phonon potential and accordingly, change in the frequency of vibrational modes. The shifting of vibrational mode towards lower frequencies sides may be related to the ion irradiation-induced distortion in the chemical bonds [36].

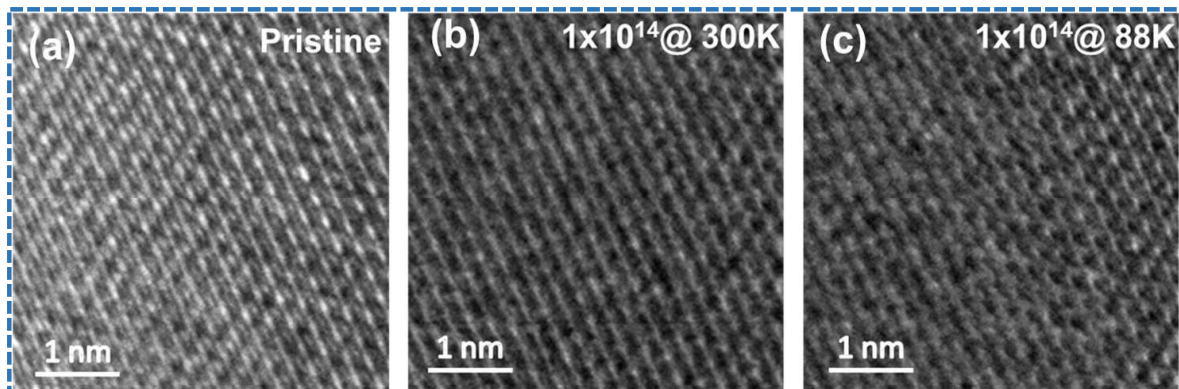


Figure 4.9 HR-TEM image of (a) un-irradiated, (b) irradiated@300K, and (c) irradiated@~88K LZO sample

Moreover, evaluating the relative change in the FWHM of the vibrational modes, we quantified the damage/amorphization in the LZO samples at ~88 K and as well as RT with the augmentation of ion fluence. The damage evaluated from the Raman spectra of LZO samples employing the equation 4.1 is presented in Table 4.1. Table 4.1 exhibits that the damage is more pronounced at ~88 K than RT, which strengthens the GIXRD results.

4.2.6 HR-TEM analysis

Fig. 4.9 (a-c) exhibits the HR-TEM photographs of pre and post-irradiated LZO samples. Fig. 4.9 (a) evidently confirmed the well-arranged atomic ordering of un-irradiated LZO samples which indicates the long-range crystallinity of samples. However, the LZO sample irradiated at RT reveals the signature of deterioration of atomic ordering [Fig. 4.9 (b)]. Further, the LZO sample irradiated at low temperature apparently affirmed the dilapidation of atomic ordering [Fig. 4.9 (c)]. Here, we would like to emphasize that the deterioration of atomic ordering of LZO samples is more significantly at low temperature than RT due to the immobile nature of defects. The HR-TEM results endorsed the GIXRD and Raman spectroscopy results.

4.3 Conclusion

The series of LZO samples was successfully prepared and irradiated (~88 K and 300 K) in a well-controlled environment with 1.0 MeV Xe⁴⁺ ions at various fluences. The microstructural study of un-irradiated LZO samples suggests that the average grain size of the LZO sample is 180 nm range. The GIXRD exhibits the deterioration of the crystallinity of LZO samples. The deterioration of the crystallinity enhanced monotonically with augmentation of fluence at both the temperatures. Rietveld refinement indicates that the lattice parameters of LZO samples enhanced with the augmentation of ion fluence. Raman spectroscopy analysis suggests the concurrently weakening and broadening of the vibrational modes of LZO samples upon irradiation and are relatively higher at ~88 K. Both, GIXRD and Raman spectroscopy indicated that the damage is more pronounced at ~ 88 K with the increment of ion fluence. The HR-TEM micrographs of LZO samples confirmed that the deterioration of atomic ordering is more pronounced at ~88 K than RT.

References

- [1] K.E. Sickafus, R.W. Grimes, J.A. Valdez, A. Cleave, M. Tang, M. Ishimaru, S.M. Corish, C.R. Stanek, B.P. Uberuaga, Radiation-induced amorphization resistance and radiation tolerance in structurally related oxides, *Nat. Mater.* 6 (2007) 217–223. <https://doi.org/10.1038/nmat1842>.
- [2] T. Omata, S. Otsuka-Yao-Matsuo, Electrical Properties of Proton-Conducting Ca²⁺Doped La₂Zr₂O₇ with a Pyrochlore-Type Structure, *J. Electrochem. Soc.* 148 (2001) E252. <https://doi.org/10.1149/1.1369370>.
- [3] S.K. Gupta, M. Abdou, P.S. Ghosh, J.P. Zuniga, E. Manoharan, H.J. Kim, Y. Mao, On comparison of luminescence properties of La₂Zr₂O₇ and La₂Hf₂O₇ nanoparticles, *J. Am. Ceram. Soc.* 103 (2020) 235–248. <https://doi.org/10.1111/jace.16693>.
- [4] F.X. Zhang, M. Lang, Z. Liu, R.C. Ewing, Pressure-induced disordering and anomalous lattice expansion in La₂Zr₂O₇ pyrochlore, *Phys. Rev. Lett.* 105 (2010) 1–4. <https://doi.org/10.1103/PhysRevLett.105.015503>.
- [5] F.X. Zhang, M. Lang, R.C. Ewing, Atomic disorder in Gd₂Zr₂O₇ pyrochlore, *Appl. Phys. Lett.* 106 (2015) 191902. <https://doi.org/10.1063/1.4921268>.
- [6] S.T. Bramwell, Spin Ice State in Frustrated Magnetic Pyrochlore Materials, *Science* (5546) 294 (2001) 1495–1501. <https://doi.org/10.1126/science.1064761>.
- [7] Z. Wang, G. Zhou, D. Jiang, S. Wang, Recent development of A₂B₂O₇ system transparent ceramics, *J. Adv. Ceram.* 7 (2018) 289–306. <https://doi.org/10.1007/s40145-018-0287-z>.
- [8] G. Ou, W. Liu, L. Yao, H. Wu, W. Pan, High conductivity of La₂Zr₂O₇ nanofibers by phase control, *J. Mater. Chem. A* 2 (2014) 1855–1861. <https://doi.org/10.1039/c3ta13465b>.
- [9] F.X. Zhang, J.W. Wang, J. Lian, M.K. Lang, U. Becker, R.C. Ewing, Phase stability and pressure dependence of defect formation in Gd₂Ti₂O₇ and Gd₂Zr₂O₇ pyrochlores, *Phys. Rev. Lett.* 100 (2008) 2–5. <https://doi.org/10.1103/PhysRevLett.100.045503>.
- [10] G.M. Mustafa, S. Atiq, S.K. Abbas, S. Riaz, S. Naseem, Tunable structural and electrical impedance properties of pyrochlores based Nd doped lanthanum zirconate nanoparticles for capacitive applications, *Ceram. Int.* 44 (2018) 2170–2177. <https://doi.org/10.1016/j.ceramint.2017.10.172>.
- [11] F.X. Zhang, M. Lang, Z. Liu, R.C. Ewing, Pressure-induced disordering and anomalous lattice expansion in La₂Zr₂O₇ pyrochlore, *Phys. Rev. Lett.* 105 (2010) 1–4. <https://doi.org/10.1103/PhysRevLett.105.015503>.

- org/10.1103/PhysRevLett.105.015503.
- [12] K. KNOTH, R. HUHNE, S. OSWALD, L. SCHULTZ, B. HOLZAPFEL, Detailed investigations on $\text{La}_2\text{Zr}_2\text{O}_7$ buffer layers for YBCO-coated conductors prepared by chemical solution deposition, *Acta Mater.* 55 (2007) 517–529. <https://doi.org/10.1016/j.actamat.2006.08.040>.
- [13] C.G. Liu, Y.H. Li, Y.D. Li, L.Y. Dong, J. Wen, D.Y. Yang, Q.L. Wei, P. Yang, First principle calculation of helium in $\text{La}_2\text{Zr}_2\text{O}_7$: Effects on structural, electronic properties and radiation tolerance, *J. Nucl. Mater.* 500 (2018) 72–80. <https://doi.org/10.1016/j.jnucmat.2017.12.024>.
- [14] A. Panghal, P.K. Kulriya, Y. Kumar, F. Singh, N.L. Singh, Investigations of atomic disorder and grain growth kinetics in polycrystalline $\text{La}_2\text{Zr}_2\text{O}_7$, *Appl. Phys. A.* 125 (2019) 428. <https://doi.org/10.1007/s00339-019-2720-8>.
- [15] A. Debelle, J.P. Crocombette, A. Boulle, A. Chartier, T. Jourdan, S. Pellegrino, D. Bachiller-Perea, D. Carpentier, J. Channagiri, T.H. Nguyen, F. Garrido, L. Thomé, Lattice strain in irradiated materials unveils a prevalent defect evolution mechanism, *Phys. Rev. Mater.* 2 (2018) 1–8. <https://doi.org/10.1103/PhysRevMaterials.2.013604>.
- [16] Q. Qing, X. Shu, D. Shao, H. Zhang, F. Chi, X. Lu, Irradiation response of $\text{Nd}_2\text{Zr}_2\text{O}_7$ under heavy ions irradiation, *J. Eur. Ceram. Soc.* 38 (2018) 2068–2073. <https://doi.org/10.1016/j.jeurceramsoc.2017.11.050>.
- [17] X. Lu, X. Shu, D. Shao, S. Chen, H. Zhang, X. Yuan, F. Chi, Radiation stability of $\text{Gd}_2\text{Zr}_2\text{O}_7$ and $\text{Nd}_2\text{Ce}_2\text{O}_7$ ceramics as nuclear waste forms, *Ceram. Int.* 44 (2018) 760–765. <https://doi.org/10.1016/j.ceramint.2017.09.244>.
- [18] G. Velişa, E. Wendler, L.L. Wang, Y. Zhang, W.J. Weber, Amorphization kinetics in strontium titanate at 16 and 300 K under argon ion irradiation, *J. Mater. Sci.* 54 (2019) 6066–6072. <https://doi.org/10.1007/s10853-018-03313-7>.
- [19] A. Chartier, C. Meis, W.J. Weber, L.R. Corrales, Theoretical study of disorder in Ti-substituted ($\text{La}_2\text{Zr}_2\text{O}_7$), *Phys. Rev. B - Condens. Matter Mater. Phys.* 65 (2002) 1–11. <https://doi.org/10.1103/PhysRevB.65.134116>.
- [20] J. Lian, X.T. Zu, K.V.G. Kutty, J. Chen, L.M. Wang, R.C. Ewing, R.C. Ewing, Ion-irradiation-induced amorphization of $\text{La}_2\text{Zr}_2\text{O}_7$ pyrochlore, *Phys. Rev. B - Condens. Matter Mater. Phys.* 66 (2002) 541081–541085. <https://doi.org/10.1103/PhysRevB.66.054108>.
- [21] P. Scardi, M. Leoni, R. Delhez, Line broadening analysis using integral breadth methods: a critical review, *J. Appl. Crystallogr.* 37 (2004) 381–390. <https://doi.org/10.1103/PhysRevB.66.054108>.

1107/S0021889804004583.

- [22] P. Kalita, S. Ghosh, U.B. Singh, P.K. Kulriya, V. Grover, R. Shukla, A.K. Tyagi, G. Sattonnay, D.K. Avasthi, Investigating the effect of material microstructure and irradiation temperature on the radiation tolerance of yttria stabilized zirconia against high energy heavy ions, *J. Appl. Phys.* 125 (2019). <https://doi.org/10.1063/1.5080934>.
- [23] Y.H. Li, Y.Q. Wang, C.P. Xu, J.A. Valdez, M. Tang, K.E. Sickafus, Microstructural evolution of the pyrochlore compound $\text{Er}_2\text{Ti}_2\text{O}_7$ induced by light ion irradiations, *Nucl. Instruments Methods Phys. Res. Sect. B Beam Interact. with Mater. Atoms.* 286 (2012) 218–222. <https://doi.org/10.1016/j.nimb.2011.12.034>.
- [24] S. Liu, T. Yang, J. Zhang, Z. Yan, Y. Lu, D. Han, C. Wang, Y. Fang, Y. Wang, Thermal effects in ion irradiated Ti_2AlC and Ti_3SiC_2 , *Nucl. Instruments Methods Phys. Res. Sect. B Beam Interact. with Mater. Atoms.* 435 (2018) 50–55. <https://doi.org/10.1016/j.nimb.2017.10.006>.
- [25] Y. Zhang, J. Lian, C.M. Wang, W. Jiang, R.C. Ewing, W.J. Weber, Ion-induced damage accumulation and electron-beam-enhanced recrystallization in SrTiO_3 , *Phys. Rev. B - Condens. Matter Mater. Phys.* 72 (2005) 1–8. <https://doi.org/10.1103/PhysRevB.72.094112>.
- [26] F. Schrempel, T. Gischkat, H. Hartung, E.-B. Kley, W. Wesch, Ion beam enhanced etching of LiNbO_3 , *Nucl. Instruments Methods Phys. Res. Sect. B Beam Interact. with Mater. Atoms.* 250 (2006) 164–168. <https://doi.org/10.1016/j.nimb.2006.04.101>.
- [27] Y. Kumar, P.M. Shirage, Highest coercivity and considerable saturation magnetization of CoFe_2O_4 nanoparticles with tunable band gap prepared by thermal decomposition approach, *J. Mater. Sci.* 52 (2017) 4840–4851. <https://doi.org/10.1007/s10853-016-0719-5>.
- [28] Y. Kumar, A. Sharma, P.M. Shirage, Impact of different morphologies of CoFe_2O_4 nanoparticles for tuning of structural, optical and magnetic properties, *J. Alloys Compd.* 778 (2019) 398–409. <https://doi.org/10.1016/j.jallcom.2018.11.128>.
- [29] Y. Kumar, A. Sharma, M.A. Ahmed, S.S. Mali, C.K. Hong, P.M. Shirage, Morphology-controlled synthesis and enhanced energy product (BH) max of CoFe_2O_4 nanoparticles, *New J. Chem.* 42 (2018) 15793–15802. <https://doi.org/10.1039/C8NJ02177E>.
- [30] W. Qin, T. Nagase, Y. Umakoshi, J.A. Szpunar, Relationship between microstrain and lattice parameter change in nanocrystalline materials, *Philos. Mag. Lett.* 88 (2008) 169–179. <https://doi.org/10.1080/09500830701840155>.
- [31] Y. Zhang, A. Debelle, A. Boule, P. Kluth, F. Tuomisto, Advanced techniques for

- characterization of ion beam modified materials, *Curr. Opin. Solid State Mater. Sci.* 19 (2015) 19–28. <https://doi.org/10.1016/j.cossms.2014.09.007>.
- [32] A.F. Fuentes, S.M. Montemayor, M. Maczka, M. Lang, R.C. Ewing, U. Amador, A Critical Review of Existing Criteria for the Prediction of Pyrochlore Formation and Stability, *Inorg. Chem.* 57 (2018) 12093–12105. <https://doi.org/10.1021/acs.inorgchem.8b01665>.
- [33] S.X. Zhang, J. Liu, H. Xie, L.J. Xu, P.P. Hu, J. Zeng, Z.Z. Li, L. Liu, W.S. Ai, P.F. Zhai, Vibrational modes in $\text{La}_2\text{Zr}_2\text{O}_7$ pyrochlore irradiated with disparate electrical energy losses, *Chinese Phys. B.* 28 (2019). <https://doi.org/10.1088/1674-1056/ab43bf>.
- [34] B.P. Mandal, N. Garg, S.M. Sharma, A.K. Tyagi, Solubility of ThO_2 in $\text{Gd}_2\text{Zr}_2\text{O}_7$ pyrochlore: XRD, SEM and Raman spectroscopic studies, *J. Nucl. Mater.* 392 (2009) 95–99. <https://doi.org/10.1016/j.jnucmat.2009.03.050>.
- [35] X. Shu, L. Fan, Y. Xie, W. Zhu, S. Pan, Y. Ding, F. Chi, Y. Wu, X. Lu, Alpha-particle irradiation effects on uranium-bearing $\text{Gd}_2\text{Zr}_2\text{O}_7$ ceramics for nuclear waste forms, *J. Eur. Ceram. Soc.* 37 (2017) 779–785. <https://doi.org/10.1016/j.jeurceramsoc.2016.09.034>.
- [36] M. Zhou, C. Hou, Y. Xie, L. Wang, X. Shu, D. Shao, X. Lu, Alpha-radiation effects of $\text{Gd}_2\text{Zr}_2\text{O}_7$ bearing simulated multi-nuclides, *J. Aust. Ceram. Soc.* 55 (2019) 831–836. <https://doi.org/10.1007/s41779-018-00297-0>.